communications biology

A Nature Portfolio journal

Article

https://doi.org/10.1038/s42003-025-09054-z

Alzheimer's Tau seeds-induced pathology enhances hippocampal extracellular diffusion

Juan Estaún-Panzano [1,5], **Anna Lovisotto** [1,5], **Claire Mazzocco** [1,5], **Carolina Piva** [1], **Morgane Darricau** [1], **Ivo Calaresu** [2], **Quentin Gresil** [3], **Vincent Planche** [1], **Benjamin Dehay** [1], **Laurent Groc** [2], **Laurent Cognet** [3,4] & **Erwan Bezard** [1] ✉

The extracellular space (ECS) is a complex, dynamic network occupying about 20% of the brain, filled with a cerebrospinal fluid-like solution rich in extracellular matrix (ECM) molecules. ECS properties regulate molecular diffusion, potentially influencing disease-associated protein spread in neurodegenerative diseases. However, its role in tau propagation remains unexplored. Using wild-type mice injected with tau seeds purified from Alzheimer's disease brain, we applied quantum dot single-particle tracking in live tissue to examine how tau pathology and inflammation influence extracellular diffusion. We observed increased diffusion associated with tau pathology in specific hippocampal regions. Additionally, diffusion profiles differed between cell-dense and cell-sparse areas. Astrocytes showed abnormal internalisation of proteoglycans, and matrix structural components were dysregulated, suggesting a link between altered ECM dynamics and enhanced diffusion. Increased diffusion and altered ECM dynamics might facilitate the spread of tau pathology.

Alzheimer's disease (AD) neuropathological changes are characterised by extracellular amyloid and senile plaques, which are mainly deposits of amyloid-beta (Aβ) peptides, and neurofibrillary tangles (NFTs), which are intracellular aggregates of hyperphosphorylated tau[1]. AD hallmarks also include the activation of astrocytes and microglia, contributing to neuroinflammation, vascular changes, synaptic degeneration, and, ultimately, neuronal loss and brain atrophy, especially in the hippocampus and neocortex[1].

The intracellular propagation and accumulation of NFTs are directly associated with neurodegeneration and cognitive decline in AD and other tauopathies[2]. The "prion-like" theory of tau propagation in AD involves the misfolding, release, and spread of tau proteins via the extracellular space (ECS), which induces the misfolding of soluble tau in recipient cells[3,4]. The ECS forms a continuous and heterogeneous network between the brain cells of tremendous morphological complexity, containing a cerebrospinal fluid-like solution enriched with extracellular matrix (ECM) molecules. Although its channels and reservoirs range from nano- to micrometres in size, they comprise approximately 20% of the brain[5].

The ECS/ECM properties directly affect how different entities diffuse among cells and likely play a role in disease-associated protein propagation[6]. Recent work in models of α-synuclein and amyloid pathology shows extracellular diffusion facilitation in neurodegenerative and non-neurodegenerative contexts[7,8]. However, there is currently no information available regarding experimental models of tauopathy.

We have addressed this issue using wild-type mice injected with tau seeds derived from the brains of patients with AD (AD-tau). Unlike transgenic mouse models overexpressing mutated tau, this model allows us to study non-cell autonomous tau pathology and the consequences of tau spreading, potentially affecting the ECS[9,10]. We focused exclusively on the hippocampus due to its early and prominent involvement in tau pathology, as well as its structural heterogeneity, characterized by both cell-dense and cell-sparse layers. This anatomical complexity provides a valuable framework for investigating how tissue architecture influences diffusion dynamics. We used semiconductor quantum dots (QDs) single particle tracking (SPT) in live tissue[11] to understand how cell damage and inflammation related to tau aggregation may affect extracellular diffusion in several parts of the hippocampus. The size of the used QDs closely resembles that of various biological macromolecules and nanoscale delivery systems like exosomes containing tau, which measure around 30 to 150 nm, commonly found in cerebrospinal fluid (CSF)[12] and AD brain[13], known to be capable of seeding pathology[14].

---

[1]Univ. Bordeaux, CNRS, Institut des Maladies Neurodégénératives, UMR 5293, Bordeaux, France. [2]Univ. Bordeaux, CNRS, Institut Interdisciplinaire de Neurosciences, UMR 5297, Bordeaux, France. [3]Univ. Bordeaux, CNRS, Laboratoire Photonique, Numérique et Nanosciences, UMR 5298, Talence, France. [4]IOGS, CNRS, Laboratoire Photonique, Numérique et Nanosciences, UMR 5298, Talence, France. [5]These authors contributed equally: Juan Estaún-Panzano, Anna Lovisotto, Claire Mazzocco. ✉e-mail: erwan.bezard@u-bordeaux.fr

This study aims to explore how tau pathology influences extracellular diffusion and matrix in the hippocampus, offering new insights into the extracellular mechanisms that may drive tau propagation in AD.

Materials and Methods

Tau extracts

Brain tissue from a 69-year-old male diagnosed with AD, Braak stage VI and Thal phase 5, was obtained from the Brain Bank GIE NeuroCEB (Pitié-Salpétrière Hospital, Paris, France), approved by the French Ministry of Higher Education and Research to collect and distribute brain samples (agreement AC-2013–1887), following French bioethical laws. According to French ethical guidelines, consent was signed by the patients or their next of kin in their name. Frontal cortex samples were prepared and characterised following the protocol described in ref. 15 and characterised by a dot blot.

The standard curve for quantification was obtained using serial dilutions of a human recombinant tau solution from 15 to 0.08 µg/ml (as described by[9]) and was probed by filter retardation assay using tau monoclonal antibody to assess the final total tau concentration of the samples.

The sample (100 µL) was spotted onto the nitrocellulose membrane. After the sample slots dried, the membrane was blocked using a blocking solution with 5% BSA in PBS for 1 hour at room temperature. The membrane was then incubated with tau monoclonal antibody (HT7, 1/1000) or Phospho-Tau (Ser202, Thr205) monoclonal antibody (AT8, 1/1000) or anti-3R or anti-4R antibodies (1/1000 diluted in PBS 0.1% Tween 20, 3% BSA), Thermo-scientific) overnight at 4 °C. Following incubation, the membrane was washed 6 times with PBS with 0.1% Tween-20. The secondary antibody (goat anti-mouse IRDye800, Li-Core 1/10000 in PBS 0.1% Tween 20, 3% BSA) was applied, and the membrane was incubated for another hour. After additional washing steps, the signal was detected on the membrane by scanning on an Odyssey Li-Core scanner at 800 nm.

Animals and modelling procedure

Experiments were performed following the European Union directive (2010/63/EU) on protecting animals used for scientific purposes. They were approved by the Ethical Committee of Bordeaux University (CE50, France) and the Ministry of Education and Research under license number APAFIS #32540-2021072016125086 v11. The study abides by ARRIVE guidelines. Surgeries were performed as previously described in ref. 7. Briefly, 8-week-old male mice ($n = 3–9$; exact number specified in the Figure legend) were unilaterally injected in the hippocampus (AP-2.54/ML −2/DV −2.4), as defined[10] with either tau seeds or phosphate buffer saline (PBS) as control. Mice were kept for 4 months before ex vivo imaging and termination.

QD SPT in acute brain slices

Mice were euthanised by cervical dislocation. Brains were swiftly extracted, and coronal sections (300-µm thick) were prepared in a VT1200S vibratome (Leica) in ice-cold NMDG solution and left to recover in NMDG solution for at least 20 min at room temperature. NMDG in mM: 93 NMDG, 2.5 KCl, 1.2 $NaH_2PO_4{\cdot}2H_20$, 20 HEPES, 25 glucose, 30 $NaHCO_3$, 10 $MgSO_4$, 0.5 $CaCl_2$. 1 Sodium Pyruvate and 12 N-acetylcysteine were added just before the experiment. pH was adjusted to 7.3–7.4 using HCl. Measured Osm 290–300. Slices were then transferred to room temperature aCSF (gassed with 95% O_2, 5% CO_2) with the following composition (in mM) 140 NaCl, 2.5 KCl, 1.2 $NaH_2PO_4{\cdot}2H_2O$, 26 $NaHCO_3$, 10 glucose, 10 HEPES, 2 $MgSO_4$, and 2 $CaCl_2$. Sodium Pyruvate and 12 N-acetylcysteine were added just before the experiment. pH was adjusted to 7.3–7.4 using HCl. The osmolarity was 300–310 mOsm [10]. After preparation and recovery, slices were then incubated for 40 min at 1 mL of QDs (ThermoFisher Scientific, Cat. #Q-11422MP) suspension (1 mM) in carbogenated aCSF (95% O_2, 5% CO_2, in mM): 126 NaCl, 3.5 KCl, 25 $NaHCO_3$, 12 glucose, 1.2 $NaH_2PO_4{\bullet}2H_20$, 1.3 $MgCl_2{\bullet}6H_20$, and 2 $CaCl_2{\bullet}2H_20$. Sodium Pyruvate and 12 N-Acetylcysteine, pH 7.3–7.4. Measured mOsm 300–310. Slices were rinsed for 8 minutes in 1 mL of bubbled QD-free aCSF before imaging. After incubation, images were collected at 35 °C in a 3D-printed chamber with controlled temperature by a feedback system. Pre-warmed carbogen-bubbled aCSF was perfused throughout the chamber by a peristaltic pump. Hippocampal regions of interest were selected within the transition zone between the anterior and medial hippocampus. Stereotaxic coordinates were determined according to the Paxinos and Franklin mouse brain atlas, targeting a range from −1.7 mm to -2.3 mm relative to bregma (3 slices per mouse). Slices were imaged for no more than 45 min. Imaging of moving QDs in the ECS was performed on a customized upright epifluorescent microscope (Nikon) using a 25x/1.10NA water-dipping objective (Nikon)[16]. QDs were excited at 488 nm (200 mW). Excitation light was separated from the emitted using a quad-band polychroic mirror (405/488/561-568/635-647, Chroma®); emitted light was further passed respectively on a 447/60 and 655/15 nm single-band bandpass filter (BrightLine®). Images were acquired were collected using a 30 ms exposure time with an sCMOS camera (Prime BSI, Teledyne). Before recording, transmission white light was used to check the position in the entire slice and determine the brain region to be imaged[14]. To avoid non-physiological data acquisition, the first 15 µm of tissue was always discarded to exclude the first cell layer, which was potentially damaged during slicing.

QD localisation and trajectory analysis

Low-resolution image stacks of single emitters were segmented, particle position was super-localized, and single molecule trajectories were reconnected with PALMtracer, a high-end software package (MetaMorph® – Molecular Devices) for the analysis of single-molecule dynamics [14]. Briefly, a wavelet segmentation and a Gaussian fitting (6 pixels around maxima) are used for threshold-based localisation. At the same time, a simulated annealing algorithm is applied for trajectory reconstruction through successive images. As a result, the mean-square displacement (MSD) of moving particles as a function of time is obtained. Only trajectories described by more than 10 points were analysed. The diffusion coefficient (D) was calculated for all trajectories through a linear fit of the first 4 points of the MSD curve. Supplementary Fig. 1 provides representative examples of individual QD trajectories, illustrating the diversity of diffusion behaviours captured across the experimental conditions. We applied filtering steps to exclude immobile particles and those moving in solution (Base-10 logarithmic values of the D coefficient ranged from $\log_{10}(2.3\ \mu m^2/s)$ to $\log_{10}(0.301\ \mu m^2/s)$. We consider the QDs as immobile when their instantaneous diffusion coefficient (Dinst) is below 0.0005 $\mu m^2/s$. At the curve plateau, between 0.6 and 0.8 s, the mean square displacement average value was used as a proxy of the confinement area experienced by QD. To improve signal quality and reduce background noise, each field of view was divided into smaller regions of interest (ROIs), within which dozens of QDs were simultaneously tracked. This strategy enabled the acquisition of hundreds of trajectories per movie, resulting in several thousand trajectories analysed for each hippocampal region. Filtering steps were applied to exclude immobile particles and those likely moving outside the tissue, ensuring that the analysed tracks reflected meaningful motion within the ECS. While individual QDs explored only a limited area during the 0.8 s tracking window, our conclusions rely on the ensemble behaviour of many short, independent trajectories. This standard approach in ECS-SPT studies allows for robust measurement of diffusivity at the population level, despite the limited sampling volume of single particles.

Immunostaining and qPCR

Animals were terminated by cardiac perfusion, and brains were swiftly extracted. Brains were fixed for 72 h in 4% PFA at 4 °C and then kept in 20% sucrose/PBS (24 h) before being frozen by immersion in a cold isopentane bath (−60 °C) for at least 1 min and stored immediately at −80 °C until sectioning in a cryostat at −20 °C. 50 µm-thick coronal sections were collected and kept in Phosphate-buffered saline (PBS1X-azide 0.2% at 4 °C before immunostaining. We focused our analysis exclusively on anterio-medial hippocampal slices (Bregma -1.7/-2.3). For immunohistochemistry, 50 µm free-floating coronal sections were blocked and permeabilised 1 h with 1% BSA + 0.3% Triton X-100 in PBS1X and incubated overnight with an appropriate primary antibody: Iba1 (Rb, 019-19741, Wako). Antibodies are also reported in Supplementary Table 1. Staining was revealed using an anti-mouse or anti-rabbit HRP EnVision kit (Dako) for 30 min followed by DAB revelation and counterstained with 0.1% cresyl violet solution when necessary. Sections were scanned in a high-resolution scanner (PanScan, 3D Histech) at ×20 magnification and Iba-1 surface was calculated using the Visiopham software by a threshold detection macro analysis.

qPCR was performed from hippocampal homogenates as described in ref. 8. Primer sequences are reported in Supplementary Table 2.

Fluorescence imaging

Labelling was achieved by blocking samples with 4% bovine serum and overnight incubation with primary antibodies for the following antigens: Iba1 (Rb, 019-19741, Wako), GFAP (Ms, MAB360, Merk Millipore), Aggrecan (Rb,13880-1-AP, Thermo Fisher), NeuN (Ms, MAB377 (clone A60), Merck Millipore). Staining was revealed with appropriate secondary antibodies conjugated with Alexa 488, 568 or 647 (Thermo Fisher). Sections were mounted on #1.5 coverslips with VECTASHIELD® Antifade Mounting Medium and left to dry overnight in darkness. Confocal images were acquired in a Leica TCS SP8 microscope with a 63X Plan Apo CS objective with oil immersion, maintaining image acquisition settings (laser power, AOTF, detection parameters) between sessions. Image stacks: pixel size: 90 nm, z-step 0.5 µm. Images were treated and analysed with Fiji/ImageJ. Wide-field images were acquired in a BX 63 Olympus microscope with a mercury lamp, using a Dry UPLFLN 10X Objective (NA 0.3). Acquisition parameters were kept between acquisitions. Analysis was performed in Image/J Fiji. ROIs were drawn manually.

Data and statistical analysis

The source data for all graphs and charts is available at Zenodo: https://doi.org/10.5281/zenodo.14999889. Statistics were performed with Graph Pad Prism 9. qPCR analysis and statistics were performed using the GEASE tool (Developed by Neurocentre Magendie, Bordeaux, France).

Ethics approval and consent to participate

Brain tissue from a 69-year-old male diagnosed with AD, Braak stage VI and Thal phase 5, was obtained from the Brain Bank GIE NeuroCEB (Pitié-Salpêtrière Hospital, Paris, France), approved by the French Ministry of Higher Education and Research to collect and distribute brain samples (agreement AC-2013–1887), following French bioethical laws. According to French ethical guidelines, consent was signed by the patients or their next of kin in their name.

Animal experiments were performed following the European Union directive (2010/63/EU) on protecting animals used for scientific purposes. They were approved by the Ethical Committee of Bordeaux University (CE50, France) and the Ministry of Education and Research under license number APAFIS #32540-2021072016125086 v11. The study abides by ARRIVE guidelines.

Reporting summary

Further information on research design is available in the Nature Portfolio Reporting Summary linked to this article.

Results

AD-tau seeds injection triggers hippocampal neurodegeneration and inflammation

We used a mouse model of hippocampal tau pathology by injecting tau seeds derived from AD brains[10], including the 3 R and 4 R isoforms (Fig. 1A, B), unilaterally into the medial hippocampus (Fig. 1C). PBS-injected mice were used as controls. Four months after administration, mice were tested to evaluate the integrity of the hippocampus. We have focused our study on the dentate gyrus (Granular cell layers (GC) + hilus) and proximal CA3 (CA3 pyramidal cells (CA3py) and CA3 oriens (CA3or)) subfields of the hippocampus. Integrated density analysis reveals a significant NeuN-positive immunofluorescence reduction in the ratio ipsilateral (ipsi) / contralateral (contra) sides compared with PBS-injected mice in the hilus and CA3 pyramidal layer (Fig. 1D, E). We also observed abundant green autofluorescent signals solely in the ipsilateral tau-injected hippocampi. These signals showed a recurrent pattern, stretching from the granular/hilar region towards the interventricular foramen and third ventricle, suggesting a transport[17] (Fig. 1D; Supplementary Figs. 2 and 3). These objects presented autofluorescence spectra matching that of lipofuscin[18] and diameters compatible with cell debris (Supplementary Fig. 2C–E). These components were typically surrounded by LAMP-1-positive structures (Fig. 1F), a common phenomenon in swollen, lipofuscin-rich, abnormal neuronal processes often found in tauopathies[19,20]. Furthermore, these cell components were usually in direct contact, sometimes swollen, with microglia processes (Fig. 1G).

Unlike Guo et al.[10], we found smaller AT-8 puncta, not tangle-like aggregates, in the DG/CA3 subfields (Fig. 1H) of tau-injected mice. Knowing that AT-8 immunoreactivity is also often associated with neuroinflammation, we next wanted to determine whether the tau seeds injections resulted in changes in microglia using Iba1 staining. We observed significant density changes of Iba-1-positive microglia in the hilus and CA3or (Fig. 1I, J). We also performed qPCR on tissue homogenates from the CA3-DG area to test the presence of pro-inflammatory and cell death-related molecules. We found significant increases in inflammation-related molecules, notably Interleukin-6 (Il-6) and the apoptosis-related marker, Caspase-3 (Cas-3) (Fig. 1K).

Together, these results show that tau-induced pathology impacts the hippocampal environment, providing a relevant context to study extracellular diffusion mechanisms.

Hippocampus ECS rheology is altered by tau-seeds injections

We next investigated diffusion dynamics in the ECS, a critical yet often overlooked factor in these conditions. We used live tissue QD SPT[11] to characterise extracellular diffusion. These particles are shielded by a PEG coating and functionalised with F(ab')2 IgG (H + L, goat anti-rabbit) fragments, dry size median = 25 nm, wet size median ₌ 34 nm, Supplementary Fig. 4). QDs' size, uniformity, and photostability enable precise movement tracking as they infiltrate the tissue and diffuse within the ECS at depths between 15-40 µm. Later analysis of video recordings involved particle super-localisation, trajectory reconstruction, and MSD analysis[11] (Fig. 2A). Each recording was assigned to one of the previously defined regions of interest (GC, hilus, Ca3py, Ca3or). We analysed ECS rheology using MSD analysis[11,16] of QD trajectories. At longer time scales (0.6–0.8 s), time-averaged MSD curves display an apparent plateau (i.e. a levelling off typical of subdiffusive behaviour) that is used as a proxy of the impact of ECS footprint on the explored areas[21]. We clarify that the apparent MSD plateau likely reflects hindered diffusion of QDs within the brain ECS over the timescales of our recordings.

We first directly compared neighbouring areas, highlighting region-specific constraints on particle motion in PBS-injected mice. Lower diffusion values and more constrained mobility were observed in cell-dense layers (Fig. 2B). Then, we moved to compare PBS-injected vs. tau-injected mice. Interestingly, tau-injected mice exhibited hallmarks of significantly expanded ECS in the hippocampus compared to PBS-injected controls (cf. MSDs plateau, Fig. 2C–F). Due to their particular glial environment and nature, we also measured QDs moving in the immediate surroundings of auto-fluorescent objects by defining a ROI of 15 µm around these objects. We observed a significantly elevated and less defined plateau, indicative of a highly disrupted ECS (Fig. 2G, H).

We further analysed QD dynamics through diffusion coefficient (D, $\mu m^2/s$) distribution[11,22], defined on a timescale of the first 120 ms of individual particle trajectories. Similar to confinement area trends, diffusion coefficients varied across experimental regions (Fig. 2I, J). The mean diffusion coefficient was significantly higher in granular and CA3 pyramidal layers of tau-injected mice compared to PBS counterparts, probably accompanying cellular degeneration (Fig. 2K). Notably, diffusion around auto-fluorescent objects was the highest, possibly due to their glial environment and a facilitated mechanism for migration and waste clearance.

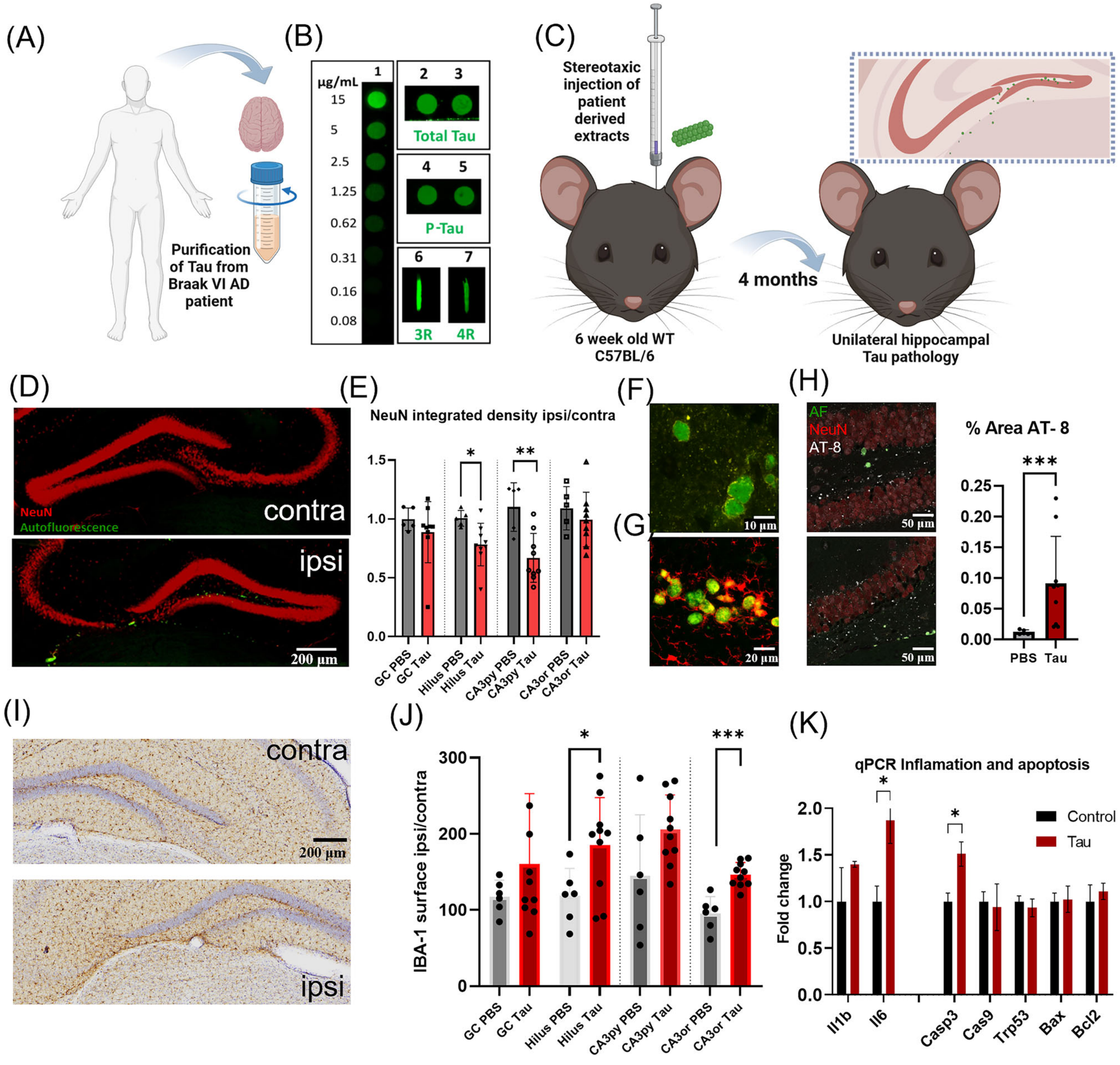

Fig. 1 | The injection of pathological tau seeds derived from patients triggers inflammatory responses and neuronal cell loss in mice. A Tau seeds were purified from the brain of Alzheimer's disease patients at Braak stage VI. **B** A filtration binding assay (dot blot) pl recombinant tau protein (ranging from 15 to 0.08 µg, 1). This method also permitted the detection of P(Ser202, Thr205)Tau in the extracts (4, 5 duplicates). The presence of both 3 R and 4 R isoforms was confirmed by slot blot (6, 7). **C** Stereotactic injection of tau extracts, or PBS was performed in mouse hippocampus[10]. Four months post-injection, animals were terminated, and their brains were used either for immunostaining analysis (*n* = 5 mice PBS, *n* = 9 mice Tau) or QDs SPT. We restrained our analysis to the granular area and proximal CA3 regions. **D** NeuN labeling of ipsi and contralateral tau-injected hippocampi. Autofluorescent (AF) signal appears in the GFP channel stretching from the granular/hilar region, extending towards the Interventricular Foramen and third ventricle. **E** Quantification of NeuN signal integrated density (Area * Mean Intensity) reveals neuronal death and/or structural atrophy: (mean ± SEM) Hilus: PBS: 1.01 ± 0.03, Tau 0.782 ± 0.06 Mann Whitney test p-value = 0.0102; Granular cells: PBS: 0.997 ± 0.043, Tau 0.888 ± 0.09 Mann Whitney test p-value = 0.24; CA3 py: PBS: 1.10 ± 0.092, Tau 0.67 ± 0.07 Mann Whitney test *p*-value = 0.007; CA3or: PBS: 1.09 ± 0.082, Tau 0.996 ± 0.077 Mann Whitney test p-value = 0.44). **F** AF objects are surrounded by the lysosomal marker LAMP-1 and are usually in direct contact, sometimes swollen with (**G**) IBA-1-positive activated microglia. **H** 63x confocal micrographs of granular (top) and CA3 pyramidal areas (bottom). The model presents AT-8 puncta exclusively in the Tau-injected mice (AT-8% Area, Mean ± SEM: PBS: 0.012 ± 0.0016, Tau = 0.092 ± 0.025, Kruskal-Wallis test *p*-value = 0.0010). **I**, **J** There is a microglial hyper-activation in our zones under study measured by IBA-1 density (%surface IBA-1 ipsi/contra (mean ± SEM) Hilus: PBS: 118.5 ± 14.8, Tau 185.1 ± 19.7 Mann Whitney test p-value = 0.042; Granular cells: PBS: 118.0 ± 8.86, Tau 160.1 ± 29.3 Mann Whitney test p-value = 0.63; CA3 py: PBS: 145.0 ± 32.8, Tau 205 ± 14.5 Mann Whitney test p-value = 0.12; CA3 or: PBS: 95.3 ± 9.1, Tau 146 ± 5.1 Mann Whitney test p-value = 0.0005). **K** qPCR on tissue homogenates extracted from CA3-DG area (n = 3 mice). We found significant increases in inflammation and apoptosis genes (Il-6 p-value = 0.038, Casp3 p-value = 0.04). Error bars represent mean ± SD. Created in BioRender. Bezard, E. (2025) https://BioRender.com/b68b484.

Taken together, our rheology data reveal notable differences between cell-dense and cell-sparse areas, while tau pathology was associated with rheological alterations, notably through an enhancement of diffusion.

Hippocampus extracellular matrix is disrupted after AD-tau seeds injection

The increased diffusion led us to investigate the ECM structure. The ECM is a dynamic structure formed mainly by hyaluronan, glycosaminoglycans

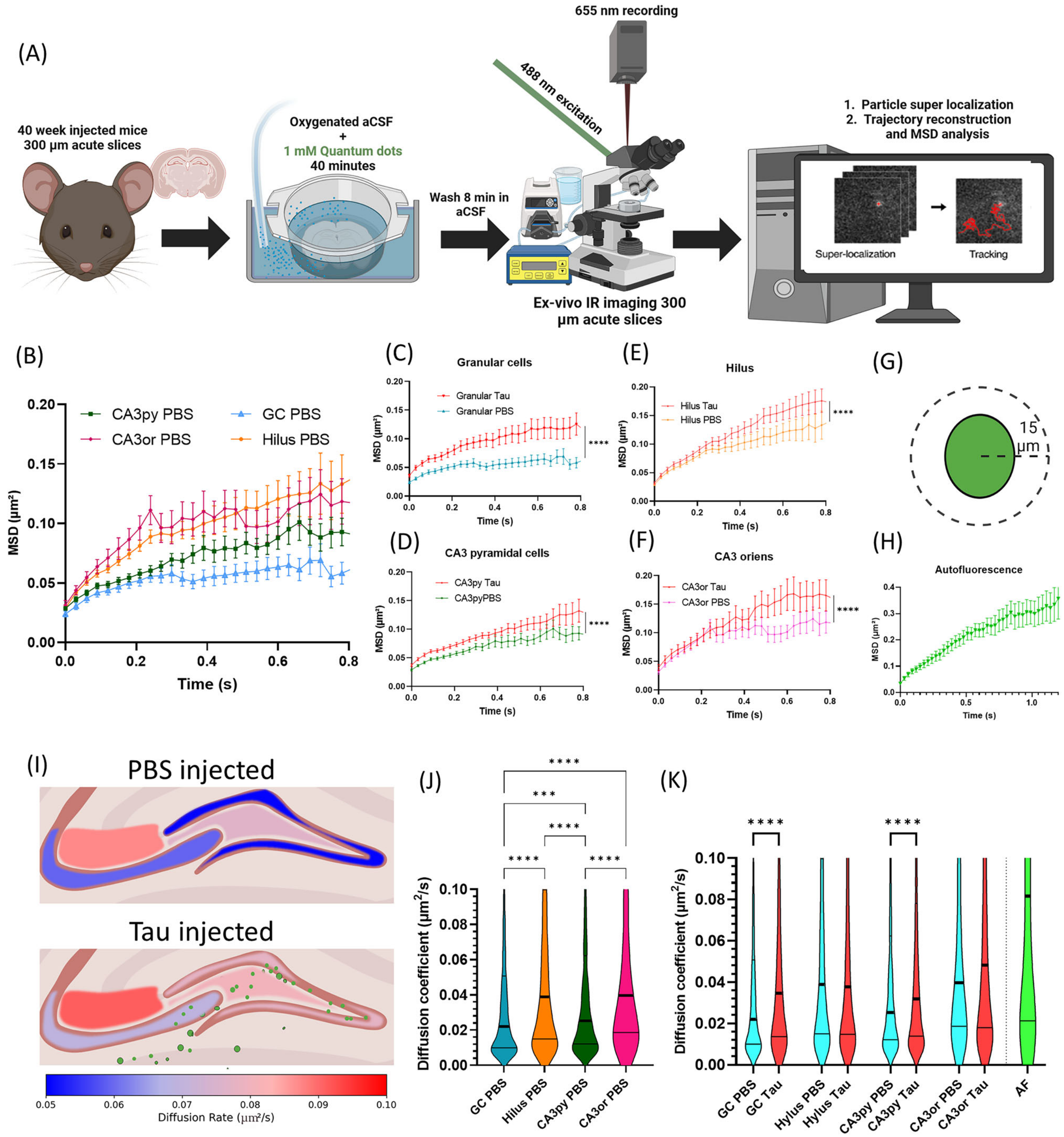

(GAGs), such as aggrecan and versican, and smaller linking proteins. ECM regulates diffusion in the ECS, usually slowing it down[5,6]. It varies in structure and density across regions (Supplementary Fig. 5), likely affecting region-specific regimes[23]. The internalisation and disruption of some of the ECM structure components are compatible with the facilitated diffusion reported here and by others in various contexts, including in the disease context[6,8,24,25].

ECM changes result from varying expression patterns and complex proteolytic processes, with alterations linked to neurological disorders[8,26]. We first investigated the abnormal internalisation of matrix structural components such as GAGs, notably aggrecan by glia. We quantified GFAP-positive pixels colocalising with aggrecan and observed significantly increased colocalisation in mice injected with AD tau-seeds, suggesting tau-induced pathology promotes excessive aggrecan internalisation by astrocytes. (Fig. 3A–C).

Next, we sought to determine whether abnormal glial matrix internalisation contributes to decreased hilar integrated density shown in (Fig. 1J). Interestingly, GFAP-aggrecan colocalisation strongly negatively correlated with hilar integrated density ($r = -0.79$, p-value = 0.0007), suggesting an abnormal matrix internalisation by astrocytes may drive hilar collapse (Supplementary Fig. 6).

We finally studied the dysregulation of key structural matrix components. A proposed mechanism driving matrix disruption is the imbalance between extracellular protease activity and ECM component expression[26,27]. We thus measured the mRNA abundance of ECM modulators by RT-qPCR, including metalloproteases and sulphatases. While metalloproteases were unchanged, we observed a significant increase in N-acetylgalactosamine 6-sulfatase (Galns), a lysosomal exohydrolase involved in the removal of sulphation motifs from certain sulphate

Fig. 2 | Extracellular diffusion is diverse in the hippocampus and is significantly enhanced by tau pathology. **A** 300 µm acute slices were prepared in ice-cold NMDG solution. After 40 min of incubation, QDs infiltrated slices and diffused extracellularly. Post-hoc analysis included particle super-localization, trajectory reconstruction, and MSD analysis. Recordings were assigned to predefined regions. **B** MSD comparison across regions shows ECS-characteristic levelling-off, indicating restricted diffusion. Plateau values (0.6–0.8 s) serve as proxies for confined areas explored by particles. Control hippocampal regions present significant differences in their MSD plateaus (μm^2, mean ± SEM (plateau 0.6-0.8 s)): Hilus PBS: 0.128 ± 0.0075 (n of videos =25, n of trajectories = 917), CG PBS = 0.063 ± 0.0035 (n of videos =14, n of trajectories = 1236), CA3py PBS: 0.093 ± 0.0042 (n of videos =21, n of trajectories = 2701), CA3or PBS = 0.116 ± 0.0065 (n of videos =9, n of trajectories = 1173), Kruskal-Wallis test p-value < 0.0001 (Dunn's multiple comparisons correction p-values: Hilus PBS vs. CA3py PBS = 0.0007, Hilus PBS vs. CA3or PBS = > 0.99, Granular PBS vs. CA3py PBS < 0.0001, Granular PBS vs. CA3or PBS < 0.0001, CA3py PBS vs. CA3or = 0.0079 (asterisks not shown in Figure)). The error bars represent the standard error of the mean (SEM) calculated across individual recordings for all trajectories at each time lag. **C–F** Comparison of PBS and Tau-injected models reveals a significant increase of MSD plateau values (μm^2, mean ± SEM plateau (0.6-0.8)): Hilus PBS: 0.128 ± 0.007 (n of videos =25, n of trajectories = 917), Tau 0.168 ± 0.006 (n of videos =37, n of trajectories = 6595) Welch's test p-value < 0.0001; CG PBS = 0.063 ± 0.003 (n of videos =14, n of trajectories = 1236), Tau 0.118 ± 0.006 (n of trajectories=28, n of trajectories = 3482) Welch's test p-value < 0.0001; CA3 py: PBS: 0.093 ± 0.004 (n of videos =21, n of trajectories = 2701), Tau 0.123 ± 0.006 (n of trajectories=34, n of trajectories = 8995) Welch's test p-value < 0.0001; CA3 or: PBS = 0.116 ± 0.006B (n of videos = 9, n of trajectories = 1173), Tau 0.165 ± 0.009 (n of trajectories=17, n of trajectories = 4658) Welch's test p-value < 0.0001). The error bars represent the standard error of the mean (SEM) calculated across individual recordings for all trajectories at each time lag. **G**, **H** MSDs around auto-fluorescent signals present a less clear plateau. Quantification renders a higher plateau value than all other conditions: 0.26 ± 0.01 (n of videos =10, n of trajectories = 1763), Kruskal-Wallis test p-value < 0.0001, Dunn's multiple comparisons test < 0.0001 for all comparisons. The error bars represent the standard error of the mean (SEM) calculated across individual recordings for all trajectories at each time lag. **I**, **J** Likewise, the diffusion coefficient distribution differs among zones. Diffusion coefficient ($\mu m^2/s$, mean ± SEM): Hilus = 0.0771 ± 0.001, granular = 0.049 ± 0.002, CA3py: 0.055 ± 0.001, CA3or = 0.088 ± 0.003, Kruskal-Wallis test p-value < 0.0001 (Dunn's multiple comparisons test, p-values: Hilus PBS vs. Granular PBS < 0.0001, Hilus PBS vs. CA3py PBS < 0.0001, Hilus PBS vs. CA3or PBS = 0.0681, Granular PBS vs. CA3py PBS = 0.0003, Granular PBS vs. CA3or PBS < 0.0001, CA3py PBS vs. CA3or PBS < 0.0001). **K** Distribution of diffusion coefficient also indicates facilitated particle movements in the Tau model brain than in WT, significant in the granular and CA3 pyramidal layers (Hilus: PBS: 0.077 ± 0.001, Tau 0.080 ± 0.001 Welch's test p-value = 0.062; Granular cells: PBS: 0.049 ± 0.002, Tau 0.078 ± 0.002 Welch's test p-value < 0.0001; CA3 py: PBS: 0.055 ± 0.001, Tau 0.068 ± 0.001 Welch's test p-value < 0.0001; CA3or: PBS: 0.088 ± 0.003, Tau 0.092 ± 0.002 Welch's test p-value = 0.32, Autofluorescence: 0.122 ± 0.005, Kruskal-Wallis test p-value < 0.0001, Dunn's multiple comparisons test < 0.00001 for all comparisons). (n = 7 mice PBS, n = 9 mice Tau). Created in BioRender. Bezard, E. (2025) https://BioRender.com/b68b484.

proteoglycans (e.g., aggrecan)[28]. Additionally, glycoprotein mRNA abundance increased, particularly versican (Fig. 3D), supporting altered matrix metabolism.

Discussion

Our results show that AD patient-derived tau seeds induce pathology characterised by neuronal cell death, inflammation, and ECM disruption. Significant changes in the rheological properties of the ECS accompany these alterations. We also report facilitated diffusion around apoptotic debris in the hippocampus. The autofluorescence pattern may indicate the transport of intracellular waste toward the ventricles, which could act as a drainage pathway for cellular waste and metabolites carried by CSF[29]. Pathology-induced gliosis leads to the internalisation of matrix components and the dysregulation of crucial metabolic components, likely contributing to both rheological and structural changes.

Noteworthy, ECS/ECM properties influence interstitial diffusion, impacting pathological protein propagation and clearance[6]. First, Suttkus et al.[30] demonstrated that the brain ECM acts as a structural scaffold that restricts the lateral mobility of membrane proteins and the diffusion of molecules in the extracellular space. Most interestingly, aggrecan was shown to generate an external barrier restricting internalization and distribution of exogenous tau in organotypic slices[28,30,31]. Building on this, Zhang et al.[32] showed that astrocytes in tauopathy models actively remodel the ECM by upregulating ECM-related genes. This astrocyte-derived ECM promotes tau aggregate propagation by enhancing fibril binding and uptake in neighbouring cells. Notably, genetic disruption of ECM pathways (e.g., *Adamts4* deletion) reduces tau spread and neurodegeneration in vivo, demonstrating a causal link between ECM remodelling and disease progression. Furthermore, Sun et al.[33] provided evidence that specific extracellular matrix components, namely heparan sulfate proteoglycans (HSPGs), mediate tau internalisation.

Using mice injected with patient-derived tau seeds, we highlight ECS rheological changes accompanying tau pathology in a setting reflecting neurodegeneration and inflammation, not just pure Tau aggregate accumulation. Compared to genetic models, our model more accurately reflects the non-cell autonomous pathophysiology of AD, with local tau seeding, distant spreading and neurodegeneration. The resulting pro-inflammation apoptotic environment contributes to accumulated cellular debris, providing a relevant context for investigating ECS rheology.

Interestingly, this experimental tau model shows increased hippocampal diffusion and ECM disruption, likely affecting tau pathology propagation[30] through, possibly, extracellular vesicles (EVs). EVs mediate protein transfer and aggregation in CNS disorders[13,34,35]. Ruan and colleagues showed that tau-containing EVs from patients with AD have vigorous local seeding activity in mice[14]. Our QDs, similar in size to EVs and tau oligomers[36,37], are expected to show comparable diffusion behaviour; however, we fully acknowledge that each nanoscale probe has distinct physicochemical properties influencing their mobility in complex biological environments. While QDs offer advantages over other probes (e.g., SWCNTs) in terms of surface functionalization and size control, limitations remain—particularly variability in surface coatings and potential for non-specific interactions. Thus, probe-dependent behaviour must be carefully considered when interpreting ECS diffusion data.

Regarding diffusion increase mechanisms, we hypothesized that the observed increase in diffusion could potentially result from tau-induced disruption of the extracellular matrix. Although we did not directly test this mechanism in the present study, previous work has shown that ECM degradation is associated with enhanced diffusion in the extracellular space[5,6,8,11,22,24,38]. Our findings should therefore be interpreted within this context and remain correlative. However, enhanced ECS diffusion in matrix-depleted regions could be explained by multiple, non-exclusive mechanisms. While matrix degradation via internalisation and remodelling is one plausible driver of increased diffusion, alternative explanations such as expansion of local ECS volume and reduction in steric or adhesive interactions with ECS boundaries are also likely contributors [31]. As previously demonstrated by Thorne and Nicholson[39], coated QDs tend to interact with the structural "walls" of the ECS rather than with ECM molecules directly; thus, matrix removal may indirectly modulate QD behaviour by altering ECS geometry and topology.

Rheological changes also affect waste clearance. Enhanced ECS diffusion may help brain cleaning by facilitating cerebrospinal and interstitial fluid movement through the glymphatic system[29]. In our model, what seem to be apoptotic bodies appear to migrate toward the ventricles, possibly benefiting from reduced ECS/ECM resistance. Activated glia likely drive these rheological changes by altering the ECM[8,25].

Does increased local diffusion worsen or hamper disease progression? Altered matrix models combined with a vesicle model[14] could be informative in answering this open question. Modelling and estimating regional

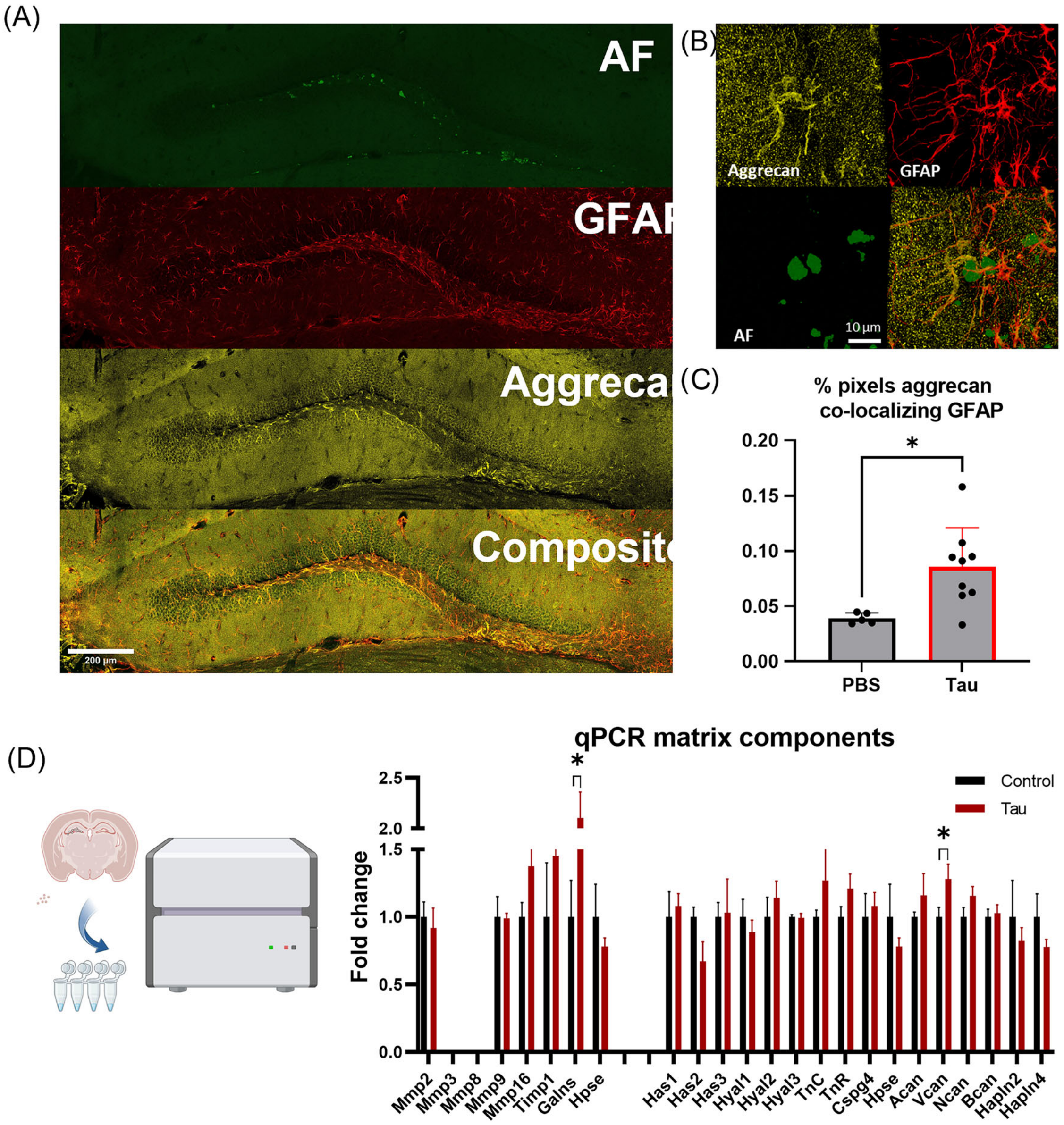

Fig. 3 | The hippocampal matrix is disrupted in tau-injected mice. **A** Aggrecan (yellow) and GFAP (red) signals overlap in specific regions, suggesting that GFAP-positive cells actively engage with and internalise the aggrecan matrix. Scale bar = 200 µm. **B** 3-D reconstruction from confocal micrographs showing an evident aggrecan internalisation by astrocytes near the AF bodies**.** **C** Manders' coefficient analysis (% of aggrecan signal overlapping with GFAP) shows significantly increased colocalisation in the tau-injected model, suggesting that GFAP-expressing cells internalise the extracellular matrix (mean ± SEM PBS = 0.039 ± 0.002, Tau = 0.08 ± 0.01, Mann-Whitney test *p*-value = 0.019). **D** qPCR shows significant upregulation of N-acetylgalactosamine 6-sulfatase (Galns) expression, which plays a key role in the degradation of GAGs. Additionally, we observed a general increase in glycoprotein mRNA levels, with a significant rise in Versican expression (Galns *p*-value = 0.026, Vcan *p*-value = 0.039). *n* = 3 mice. Error bars represent mean ± SD. Created in BioRender. Bezard, E. (2025) https://BioRender.com/b68b484.

vulnerability to tau pathology would also benefit from considering different rheology depending on the brain region and state of disease[40].

As a limitation, we acknowledge that ECS diffusion measurements are inherently probe-dependent. Given the approximate size overlap between our QDs, EVs, and tau oligomers[19,36] we infer that QDs capture some aspects of EV-like diffusion. However, smaller molecules such as neurotransmitters or ions may exhibit significantly different behaviours in the same ECS environment. This limitation underscores the importance of complementing our QD-based diffusion assay with QDs of varying sizes and surface chemistries, as well as incorporating other biophysical measurements.

Since the primary aim of this study was to determine whether alteration in diffusion and extracellular space occurs, we focused our experiments on a single time point (4 months post-injection). This time point reflects a pronounced pathology, including neuronal loss and inflammation, indicative of an advanced stage of disease. We believe future studies should investigate multiple time points and modify the ECM composition to gain deeper insight into the temporal evolution of these changes and their relationship to pathology.

Conclusions

We found an increase in extracellular diffusion in the hippocampus of the Tau model. Ultimately, ECS rheological changes are critical for understanding disease progression and treatment strategies. Local diffusion and interactions with the ECM may influence the spread of pathology and therapeutic delivery[41]. Our findings offer insights into the reorganisation of ECS rheology in tau pathology, highlighting its significance for neurodegenerative research and potential therapeutic strategies.

Data availability

The datasets used and/or analysed during the current study are available from the corresponding author on reasonable request.

Received: 13 May 2025; Accepted: 14 October 2025;

References

1. Better, M. A. Alzheimer's disease facts and figures. *Alzheimers Dement* **19**, 1598–1695 (2023).
2. Bejanin, A. et al. Tau pathology and neurodegeneration contribute to cognitive impairment in Alzheimer's disease. *Brain* **140**, 3286–3300 (2017).
3. Holmes, B. B. et al. Proteopathic tau seeding predicts tauopathy in vivo. *Proc. Natl Acad. Sci.* **111**, E4376–E4385 (2014).
4. Goedert, M., Eisenberg, D. S. & Crowther, R. A. Propagation of tau aggregates and neurodegeneration. *Annu. Rev. Neurosci.* **40**, 189–210 (2017).
5. Syková, E. & Nicholson, C. Diffusion in brain extracellular space. *Physiological Rev.* **88**, 1277–1340 (2008).
6. Tønnesen, J., Hrabětová, S. & Soria, F. N. Local diffusion in the extracellular space of the brain. *Neurobiol. Dis.* **177**, 105981 (2023).
7. Estaun-Panzano, J. et al. Intracellular α-synuclein assemblies are sufficient to alter nanoscale diffusion in the striatal extracellular space. *npj Parkinson's Dis.* **10**, 236 (2024).
8. Soria, F. N. et al. Synucleinopathy alters nanoscale organization and diffusion in the brain extracellular space through hyaluronan remodeling. *Nat. Commun.* **11**, 3440 (2020).
9. Darricau, M. et al. Tau seeds from Alzheimer's disease brains trigger tau spread in macaques while oligomeric-Aβ mediates pathology maturation. *Alzheimer's Dement.* **20**, 1894–1912 (2024).
10. Guo, J. L. et al. Unique pathological tau conformers from Alzheimer's brains transmit tau pathology in nontransgenic mice. *J. Exp. Med.* **213**, 2635–2654 (2016).
11. Grassi, D. et al. Nanoscale and functional heterogeneity of the hippocampal extracellular space. *Cell Rep.* **42**, 112478 (2023).
12. You, Y. & Ikezu, T. Emerging roles of extracellular vesicles in neurodegenerative disorders. *Neurobiol. Dis.* **130**, 104512 (2019).
13. Fowler, S. L. et al. Tau filaments are tethered within brain extracellular vesicles in Alzheimer's disease. *Nat. Neurosci.* **28**, 40–48 (2024).
14. Ruan, Z. et al. Alzheimer's disease brain-derived extracellular vesicles spread tau pathology in interneurons. *Brain* **144**, 288–309 (2021).
15. Darricau, M. et al. Tau seeds from patients induce progressive supranuclear palsy pathology and symptoms in primates. *Brain* **146**, 2524–2534 (2023).
16. Paviolo, C. et al. Nanoscale exploration of the extracellular space in the live brain by combining single carbon nanotube tracking and super-resolution imaging analysis. *Methods* **174**, 91–99 (2020).
17. Bedussi, B. et al. Clearance from the mouse brain by convection of interstitial fluid towards the ventricular system. *Fluids Barriers CNS* **12**, 1–13 (2015).
18. Haralampus-Grynaviski, N. M. et al. Spectroscopic and morphological studies of human retinal lipofuscin granules. *Proc. Natl Acad. Sci.* **100**, 3179–3184 (2003).
19. Caballero, B. et al. Acetylated tau inhibits chaperone-mediated autophagy and promotes tau pathology propagation in mice. *Nat. Commun.* **12**, 2238 (2021).
20. Barrachina, M., Maes, T., Buesa, C. & Ferrer, I. Lysosome-associated membrane protein 1 (LAMP-1) in Alzheimer's disease. *Neuropathol. Appl. Neurobiol.* **32**, 505–516 (2006).
21. Biermann, B. et al. Imaging of molecular surface dynamics in brain slices using single-particle tracking. *Nat. Commun.* **5**, 3024 (2014).
22. Godin, A. G. et al. Single-nanotube tracking reveals the nanoscale organization of the extracellular space in the live brain. *Nat. Nanotechnol.* **12**, 238–243 (2017).
23. Nicholson, C. & Hrabětová, S. Brain extracellular space: the final frontier of neuroscience. *Biophysical J.* **113**, 2133–2142 (2017).
24. Wang, L. et al. Mapping Extracellular Space Features of Viral Encephalitis to Evaluate the Proficiency of Anti-Viral Drugs. *Adv. Mater.* **36**, 2311457 (2024).
25. Hrabětová, S., Masri, D., Tao, L., Xiao, F. & Nicholson, C. Calcium diffusion enhanced after cleavage of negatively charged components of brain extracellular matrix by chondroitinase ABC. *J. Physiol.* **587**, 4029–4049 (2009).
26. Soles, A. et al. Extracellular Matrix Regulation in Physiology and in Brain Disease. *Int. J. Mol. Sci.* **24**, 7049 (2023).
27. Ulbrich, P., Khoshneviszadeh, M., Jandke, S., Schreiber, S. & Dityatev, A. Interplay between perivascular and perineuronal extracellular matrix remodelling in neurological and psychiatric diseases. *Eur. J. Neurosci.* **53**, 3811–3830 (2021).
28. Nowicka, D. & Gręda, A. Chondroitin sulfate metabolism in the brain. *Acta Neurobiologiae Experimentalis* **79**, 338–351 (2019).
29. Murdock, M. H. et al. Multisensory gamma stimulation promotes glymphatic clearance of amyloid. *Nature* **627**, 149–156 (2024).
30. Suttkus, A., Holzer, M., Morawski, M. & Arendt, T. The neuronal extracellular matrix restricts distribution and internalization of aggregated Tau-protein. *Neuroscience* **313**, 225–235 (2016).
31. Suttkus, A. et al. Aggrecan, link protein and tenascin-R are essential components of the perineuronal net to protect neurons against iron-induced oxidative stress. *Cell Death Dis.* **5**, e1119 (2014).
32. Zhang, Y. H. et al. AβPP-tau-HAS1 axis trigger HAS1-related nuclear speckles and gene transcription in Alzheimer's disease. *Matrix Biol.* **129**, 29–43 (2024).
33. Sun, Y. et al. Role of the Extracellular Matrix in Alzheimer's Disease. *Front Aging Neurosci.* **13**, 707466 (2021).
34. Li, Z. et al. Research progress on the role of extracellular vesicles in neurodegenerative diseases. *Transl. neurodegeneration* **12**, 43 (2023).
35. Thompson, A. G. et al. Extracellular vesicles in neurodegenerative disease—pathogenesis to biomarkers. *Nat. Rev. Neurol.* **12**, 346–357 (2016).
36. Fowler, S. L. et al. Tau filaments are tethered within brain extracellular vesicles in Alzheimer's disease. *Nat. Neurosci.* **28**, 40–48 (2025).
37. Lasagna-Reeves, C. A. et al. Alzheimer brain-derived tau oligomers propagate pathology from endogenous tau. *Sci. Rep.* **2**, 700 (2012).
38. Arranz, A. M. et al. Hyaluronan deficiency due to Has3 knock-out causes altered neuronal activity and seizures via reduction in brain extracellular space. *J. Neurosci.* **34**, 6164–6176 (2014).
39. Thorne, R. G. & Nicholson, C. In vivo diffusion analysis with quantum dots and dextrans predicts the width of brain extracellular space. *Proc. Natl Acad. Sci. USA* **103**, 5567–5572 (2006).
40. Cornblath, E. J. et al. Computational modeling of tau pathology spread reveals patterns of regional vulnerability and the impact of a genetic risk factor. *Sci. Adv.* **7**, eabg6677 (2021).
41. Wolak, D. J. & Thorne, R. G. Diffusion of macromolecules in the brain: implications for drug delivery. *Mol. pharmaceutics* **10**, 1492–1504 (2013).

Acknowledgements

We thank PIV-EXPE colleagues for animal care. We thank Remi Kinet and Marie-Laure Arotcarena for their helpful discussions. This study received funding from the European Research Council (ERC) under the European Union's Horizon 2020 research and innovation program (Grant agreement No. #951294 to EB, LG, and LC) and financial support from the French government in the framework of the University of Bordeaux's IdEx "Investments for the Future" program/GPR BRAIN_2030.

Author contributions

J.E.P., A.L., and C.P. carried out single-QD tracking experiments and analysed the QDs SPT. C.M. conceptualised and prepared animal models. B.D. and V.P. extracted and purified samples from patients. J.E.P., A.L., and C.P. performed immunostainings and confocal imaging. J.E.P. performed

confocal/wide-field imaging and analysis. M.D. performed Tau fibrils immunoblotting. I.C. developed the method and characterised quantum dots. Q.G. and L.C. built and validated the QDs experimental setup. L.C. L.G., and E.B. secured funding and coordinated the project. J.E.P. and E.B. conceptualised the experiments and drafted the first version of the manuscript. All authors commented on and approved the final version.

Competing interests

E.B. is the Chief Scientific Officer of Motac Neuroscience Ltd. During the past 3 years, V.P. was a local unpaid investigator or sub-investigator for clinical trials granted by NovoNordisk, Biogen, TauRx Pharmaceuticals, Janssen, Green Valley Pharmaceuticals, and Alector. He received consultant fees for animal studies from Motac Neuroscience Ltd, outside the submitted work. He received grants from the Agence Nationale de la Recherche, Fondation Recherche Alzheimer and Fondation PSP France. All other authors declare no competing interests.

Additional information

Supplementary information The online version contains supplementary material available at https://doi.org/10.1038/s42003-025-09054-z.

Correspondence and requests for materials should be addressed to Erwan Bezard.

Peer review information *Communications Biology* thanks Charles Nicholson and the other, anonymous, reviewer(s) for their contribution to the peer review of this work. Primary Handling Editor: Benjamin Bessieres. [A peer review file is available].